

Quasiparticle Spectra in the Hubbard Model.

William H. Beere and James F. Annett

University of Bristol, H.H Wills Physics Laboratory,

Royal Fort, Tyndall Avenue, Bristol BS8 1TL, UK

Abstract

We examine the quasiparticle lifetime and spectral weight near the Fermi surface in the two-dimensional Hubbard model. We use the FLEX approximation to self-consistently generate the Matsubara Green's functions and then we analytically continue to the real axis to obtain the quasiparticle spectral functions. We compare the spectral functions found in the nearest neighbor hopping only Hubbard model with those found when the second neighbor hopping is included. This separates the effects of nesting, the van Hove singularity and short-ranged antiferromagnetic correlations. The quasiparticle scattering rate is enhanced along the $(0, \pi)$ to $(\pi, 0)$ Brillouin zone diagonal. When the density is close to half-filling these 'hot spots' lie on the Fermi surface and the scattering rate increases with decreasing temperature. For the next-nearest neighbor hopping scenario we observe a large range of doping where there is no antiferromagnetism but the scattering rate has a linear temperature dependence. On decreasing the interaction this non-Fermi liquid behavior is confined to doping levels where the Fermi energy lies near the Van Hove singularity. We conclude that the 'hot spots' are associated with the antiferromagnetic phase transition while the linear temperature dependence of the scattering rate is associated with the Van Hove singularity.

Typeset using REVTeX

I. INTRODUCTION

The Hubbard model [1] is one of the simplest models for electronic correlations in solids and yet it is still not fully understood. If the electron-electron interaction strength, U , is positive and small compared to the electronic band-width, W , the model is generally expected to have a normal Fermi liquid ground state in two or three dimensions [2]. At higher U/W a number of different phases may exist, including: an antiferromagnetic insulator state, ferromagnetism, and d-wave superconductivity [3,4]. It was also proposed that in two-dimensions metallic non-Fermi liquid states may exist at large U/W , such as the resonant-valence-bond (RVB) [5] or Luttinger liquid [6] state, and the flux-phase [7]. Whether or not these phases actually exist as stable ground states of the Hubbard model remains controversial, despite considerable numerical and analytic effort to solve the two dimensional Hubbard model. Similarly, whether or not d-wave superconductivity occurs in the positive U Hubbard model is also unclear at the present time. Of course both non-Fermi liquid behavior and d-wave superconductivity appear to occur experimentally in the cuprates [8,9], where it is generally believed that the Hubbard model is appropriate. Indeed the two-dimensional Hubbard model can be derived for the cuprates from the *ab initio* density functional electronic structure under certain simplifying assumptions [10]. However it still remains unclear whether the Hubbard model is sufficient to explain all of the anomalous properties of the cuprates, or whether one must also include physical effects beyond the Hubbard Hamiltonian, such as electron-phonon coupling or multiple electronic bands.

In this paper we use the fluctuation exchange approximation [11], FLEX, to investigate the electronic structure and phase diagram for the two-dimensional Hubbard model. We pay particular attention to the antiferromagnetic (AFM) phase and the effect of antiferromagnetic fluctuations near to the AFM transition. The theory of nearly-antiferromagnetic Fermi liquids has been recently developed by Pines and co-workers [17]. Although based upon a Fermi liquid approach, the theory explains some of the non-Fermi liquid like properties of the cuprates in terms of the appearance of ‘hot spots’ on the Fermi surface where

the quasiparticle scattering rate is unusually high. Altmann, Brenig and Kampf [18] have recently shown that the FLEX approximation is able to describe these ‘hot spots’. Below we investigate in detail the regions of parameter space (e.g. temperature, T , band filling, n , and hopping t'/t) where these ‘hot spots’ occur.

A second experimental feature of the cuprates is the appearance of a temperature scale T^* (or more than one such temperature scale) distinct from both the Néel temperature T_N and the superconducting transition temperature T_c . Below T^* a loss of spectral weight occurs in the low energy excitations, referred to as a pseudogap or spin-gap [19,20]. The pseudogap can be seen directly in the angle resolved photoemission experiments [21] (ARPES) as a small k -dependent shift of the spectral edge relative to an absolute reference such as a good metal in electrical contact with the superconductor. Below we discuss the appearance of both T^* and the pseudogap in terms of the FLEX calculations for the Hubbard model.

Finally we also examine in detail the effects of the Van Hove singularity in the density of states in the two dimensional Hubbard model. The existence of van Hove singularities close to the Fermi energy is a feature of *ab initio* band structures of the cuprates [22]. The presence of the Van Hove singularity near to the Fermi surface can lead to a dramatic increase in T_c as a function of doping [23,24]. The proximity to the Van Hove singularity can also be a source of non-Fermi liquid electron-electron scattering rates. We show below that the ‘hot spots’ and the T^* behavior are associated with the antiferromagnetism, while the approximately linear in T scattering rate derives from the proximity to the Van Hove singularity. At small U (and $t' \neq 0$) these two effects exist quite separately at different band fillings, while at larger U (or $t' = 0$) both effects coexist for a wide range of doping levels.

II. THE FLUCTUATION EXCHANGE APPROXIMATION

The FLEX method was originally introduced by Bickers and Scalapino [11]. It has been discussed by many previous authors [12–15], so we present only a brief outline. FLEX makes use of the similarity of the ‘ladder’ diagrams to the ‘bubble’ diagrams from RPA when the

electron-electron interaction is an on-site interaction, as in the Hubbard model:

$$\hat{H} = \sum_{\langle ij \rangle, \sigma} t_{ij} c_{i\sigma}^\dagger c_{j\sigma} + U \sum_i n_{i\uparrow} n_{i\downarrow}. \quad (1)$$

FLEX sums both the ladder and RPA bubble diagrams, it is exact to order U^3 (while RPA is only exact to $O(U^2)$) and is a conserving approximation in the sense of Baym [16].

The electron Green's function is given by,

$$G(\mathbf{k}, i\omega_n) = \frac{1}{i\omega_n - \xi_{\mathbf{k}} - \Sigma(\mathbf{k}, i\omega_n)}, \quad (2)$$

where $\omega_n = 2\pi(n + 1/2)T$ is the Matsubara frequency, T the temperature, $\Sigma(\mathbf{k}, i\omega_n)$ the self-energy and $\xi_{\mathbf{k}}$ is the non-interacting band energy. For a 2d Hubbard model system with nearest and next-nearest neighbor hopping t_{ij} this is given by,

$$\xi_{\mathbf{k}} = -2t [\cos(k_x) + \cos(k_y)] - 4t' \cos(k_x) \cos(k_y) - \mu, \quad (3)$$

where t is the nearest neighbor hopping energy, t' the next-nearest neighbor hopping energy and μ is the chemical potential.

For FLEX both the particle-particle and particle-hole pair correlators need to be calculated, as

$$\chi^{ph}(\mathbf{q}, i\omega_m) = -\frac{1}{T} \sum_{\omega_n} \int d^2k G(\mathbf{k}, i\omega_n) G(\mathbf{q} + \mathbf{k}, i\omega_m + i\omega_n) \quad (4)$$

$$\chi^{pp}(\mathbf{q}, i\omega_m) = \frac{1}{T} \sum_{\omega_n} \int d^2k G(\mathbf{k}, i\omega_n) G(\mathbf{q} - \mathbf{k}, i\omega_m - i\omega_n). \quad (5)$$

The FLEX approximation for the self-energy is then given by,

$$\begin{aligned} \Sigma(\mathbf{k}, i\omega_n) = & \sum_{\omega_m} \int d^2q \left[G(\mathbf{k} - \mathbf{q}, i\omega_n - i\omega_m) V^{(2)}(\mathbf{q}, i\omega_m) \right. \\ & + G(\mathbf{k} - \mathbf{q}, i\omega_n - i\omega_m) V^{(ph)}(\mathbf{q}, i\omega_m) \\ & \left. + G(-\mathbf{k} + \mathbf{q}, -i\omega_n + i\omega_m) V^{(pp)}(\mathbf{q}, i\omega_m) \right]. \end{aligned} \quad (6)$$

Following Bickers and Scalapino the interaction vertices, $V^{(2)}$, $V^{(ph)}$ and $V^{(pp)}$ are given by,

$$V^{(2)}(\mathbf{q}, i\omega_m) = U^2 \chi^{ph}(\mathbf{q}, i\omega_m) \quad (7)$$

$$V^{(ph)}(\mathbf{q}, i\omega_m) = \frac{1}{2} U^2 \chi^{ph}(\mathbf{q}, i\omega_m) \left[\frac{1}{1 + U \chi^{ph}(\mathbf{q}, i\omega_m)} - 1 \right] \\ + \frac{3}{2} U^2 \chi^{ph}(\mathbf{q}, i\omega_m) \left[\frac{1}{1 - U \chi^{ph}(\mathbf{q}, i\omega_m)} - 1 \right] \quad (8)$$

$$V^{(pp)}(\mathbf{q}, i\omega_m) = -U^2 \chi^{pp}(\mathbf{q}, i\omega_m) \left[\frac{1}{1 + U \chi^{pp}(\mathbf{q}, i\omega_m)} - 1 \right]. \quad (9)$$

Note that some authors have used a modified version of FLEX in which the particle-particle channel scattering is suppressed [18]. The close similarity of our numerical results to theirs suggests that the effects of the particle-particle channel are relatively minor. The Hartree-Fock terms have been omitted from these equations as the constant term which they produce has been explicitly incorporated into the chemical potential.

Using the above set of equations we have suppressed antiferromagnetic ordering by including only matrix elements diagonal in spin space. Nevertheless we can still calculate the antiferromagnetic ordering temperature within FLEX, since the instability of the paramagnetic state is given by a Stoner like criterion:

$$U \chi^{ph}(\mathbf{Q}_{AF}, 0) > 1. \quad (10)$$

Here the antiferromagnetic ordering wave vector is given by $\mathbf{Q}_{AF} = (\pi, \pi)$, which is the position of the main peak in χ^{ph} . In all cases we only show results obtained in the ‘normal’ metallic state computed outside of the antiferromagnetic phase, given by Eq. 10. We assume that our calculations are outside any superconducting regions in the phase diagram.

The system of equations Eqs. 2-9 form a self-consistent set. The Brillouin zone integrals were discretized and we used either a 32×32 or 64×64 grid depending on the accuracy required. The Matsubara frequency sums were typically carried out using 1024 points. For temperatures of $0.06t$ this relates to a Matsubara frequency cut-off of about $\pm 200t$. All of the momentum and frequency convolutions in Eqs. 4, 5, 6 were done using fast Fourier transforms. The frequency convolution leads to high frequency errors in the correlation functions and the self-energy, but this does not produce significant errors in the final low frequency part of the Green’s function.

In order to obtain the real frequency spectral function $A(\mathbf{k}, \omega)$,

$$A(\mathbf{k}, \omega) = -\frac{1}{\pi} \text{Im}G(\mathbf{k}, \omega + i\epsilon). \quad (11)$$

the Green's functions were analytically continued from the Matsubara frequencies to the real axis. To do this we fit the Green's functions to a continued fraction of the form

$$G(z) = \frac{a_1}{1 + \frac{a_2(z - z_1)}{1 + \frac{\dots}{1 + a_N(z - z_{N-1})}}} \quad (12)$$

where the coefficients a_n are determined from the known Green's function for the positive Matsubara frequencies $z_1 = i\omega_0$, $z_2 = i\omega_1$ etc. [25]. Typically we used up to 512 terms in the continued fraction. The continued fraction approximant for $G(z)$ defines the retarded Green's function in the upper-half plane. Evaluating this on the real axis then gives $G(\omega + i\epsilon)$ and hence the spectral function, $A(\mathbf{k}, \omega)$.

The chemical potential, μ , was kept fixed during the self-consistent runs, and then the band filling, $\langle n \rangle$, was calculated from the final Green's function

$$\langle n \rangle = -\sum_{\omega_n} \int d^2k \left(\frac{1}{2} + G(\mathbf{k}, i\omega_n) \right). \quad (13)$$

This greatly speeded up the calculations compared to adjusting μ at each iteration during the self-consistency cycle in order to maintain a given density $\langle n \rangle$. Because the $\langle n \rangle$ changes slightly at a function of T for fixed μ this leads to small changes in density as a function of T . For example the case where $t' = 0$ and $\mu = .8$ the densities for temperatures of $T = .03t$ and $T = .25t$ were $\langle n \rangle = 1.18$ and $\langle n \rangle = 1.19$ respectively. These small changes in the density do not significantly alter our results.

In order to investigate the effects of the electronic band structure of the cuprates we performed calculations for both the nearest neighbor hopping only Hubbard model ($t' = 0$), and for a more realistic cuprate band structure of $t' = -0.3t$. In the case $t' = 0$ we concentrated our attention on the region near to half filling, $\langle n \rangle = 1$, and to an interaction strength of $U = 4t$. Exactly at half filling the Fermi surface is perfectly nested along \mathbf{Q}_{AF} ,

and this also coincides with the Van Hove singularity in the density of states. It is difficult therefore to distinguish the relative importance of nesting and the Van Hove singularity. However, in the case where $t' \neq 0$ the Fermi surface does not have perfect nesting at any filling, and the Van Hove singularity occurs at a finite doping. In this case we examined in detail both the region of doping around half filling and the region around the Van Hove singularity. We also compared the different effects of electron or hole doping, $\langle n \rangle > 1$ or $\langle n \rangle < 1$ respectively, corresponding to the n and p type cuprate superconductors.

III. ANALYSIS OF THE SPECTRAL FUNCTIONS

Figures 1(a,b,c) show a typical series of spectral functions, $A(\mathbf{k}, \omega)$. They illustrate the dispersion of the quasiparticle peak along the Brillouin zone lines $\mathbf{k} = (0, 0) - (\pi, 0)$, $\mathbf{k} = (\pi, 0) - (\pi, \pi)$, and $\mathbf{k} = (0, 0) - (\pi, \pi)$. In this case $t' = 0$, $U = 4t$, $T = .1t$ and the band filling was $\langle n \rangle = 1.079$. The spectral functions in the figure show a rather broad quasiparticle peak which disperses as a function of \mathbf{k} . In Figs. 1(b,c) the peak narrows and then broadens again upon passing through the Fermi surface. On the other hand, in Fig. 1(a) the peak is always broad. This is expected since the Fermi surface does not intersect the line $\mathbf{k} = (0, 0) - (\pi, 0)$ at this band filling. Overall the qualitative behavior of the spectral function is thus similar to that expected in a Fermi liquid.

A more precise quantitative analysis of the spectral functions presents some difficulties. While the quasiparticle peak is quite well defined for most of the spectra, especially near the Fermi surface, in many cases the peak is very broad and there is no clear separation between the coherent quasiparticle peak and the incoherent background. The peaks tend to be asymmetric rather than ideal Lorentzians. It can also be seen in Fig. 1(b) that the sharpest peak is not always centered at zero energy, the location of the Fermi surface. Furthermore one can also see from the figure that that the peak centered at zero energy does not have equal areas on either side of zero. This means that this Fermi surface peak does not correspond to the momentum where the occupation number equals one half. The

occupation number is essentially given by the area under the graph at negative frequencies,

$$\langle n_{\mathbf{k}} \rangle = \int A(\mathbf{k}, \omega) f(\omega) d\omega \quad (14)$$

where $f(\omega)$ is the Fermi distribution. Because of these ambiguities it is not even clear which peak corresponds to the Fermi surface crossing. The problem of locating the Fermi surface from the spectra is discussed in the following section. In the remainder of this section we concentrate on how to extract quantitative information about the quasiparticle states from the individual spectral functions.

In order to make a more detailed analysis of the spectral functions it is necessary to extract the coherent quasiparticle part of the spectrum defined by,

$$A(\mathbf{k}, \omega) = \frac{1}{\pi} \text{Im} \left[\frac{1}{(\omega - \epsilon_{\mathbf{k}})/Z_{\mathbf{k}} - i\Gamma_{\mathbf{k}}} \right]. \quad (15)$$

Fitting the quasiparticle peak in the spectrum to this Lorentzian form one can obtain the quasiparticle band energy, $\epsilon_{\mathbf{k}}$, scattering energy, $\Gamma_{\mathbf{k}}$, and spectral weight $Z_{\mathbf{k}}$. A typical such Lorentzian fit is shown in Fig. 2. Performing fits like this on each spectral function $A(\mathbf{k}, \omega)$ defines the parameters $\epsilon_{\mathbf{k}}$, $\Gamma_{\mathbf{k}}$ and $Z_{\mathbf{k}}$ throughout the Brillouin zone. It is clear from Fig. 2 that the Lorentzian fit to the spectral function gives a good approximation to the peak overall, but the fitted Lorentzian decays faster than the numerical function. There is also a slight asymmetry. These differences are usually described as the incoherent part of the spectrum. The peak is quite Lorentzian in shape and the fitting parameters are generally well defined when the peak is narrow and symmetrical, but the fitting parameters are more ambiguous when the spectral peak is broad or lop-sided.

In order to avoid these ambiguities in fitting the peak we define the quasiparticle parameters in terms of the self-energy. We calculate the real-axis self-energy from the analytic continuation of the Green's function

$$\Sigma(\mathbf{k}, \omega) = \omega - \xi_{\mathbf{k}} - \frac{1}{G(\mathbf{k}, \omega)}. \quad (16)$$

This definition of $\Sigma(\mathbf{k}, \omega)$ is more accurate than performing a separate analytic continuation of the $\Sigma(i\omega_n)$ to the real axis. Figure 3 shows the Green's function and self energy for a

point near the Fermi surface crossing. As can be seen from the figure, the imaginary part of the self-energy, although not constant, is slowly varying around the region of the spectral function peak (where $-\text{Im}[G(\omega)]$ is maximum in Fig. 3). Also the real part of the self-energy is not precisely linear in frequency over the width of the peak. For these reasons the spectral function peak is not an ideal Lorentzian. In Fermi liquid theory one takes the limits $\epsilon_{\mathbf{k}} \rightarrow 0$ and $T \rightarrow 0$ so that the quasiparticle peak is much narrower than the range of frequencies over which $\text{Re}[\Sigma]$ and $\text{Im}[\Sigma]$ vary. However at the temperatures and momentum resolutions we can access numerically (and these correspond to reasonable physical temperatures in the cuprates, eg. 100K) the quasiparticle peaks are wider than the energy scale of variations in the self-energy. We shall show below that this leads to significant deviations from Fermi liquid theory.

In order to avoid ambiguities arising from the Lorentzian fits we define the quasiparticle parameters $\epsilon_{\mathbf{k}}$, $\Gamma_{\mathbf{k}}$ and $Z_{\mathbf{k}}$ from the self-energy. The band energy is given by the solution of:

$$\text{Re}[\Sigma(\mathbf{k}, \epsilon_{\mathbf{k}})] = \epsilon_{\mathbf{k}} - \xi_{\mathbf{k}}, \quad (17)$$

which corresponds to the frequency where $\text{Re}[G(\mathbf{k}, \omega)] = 0$ in Fig. 3. The quasiparticle scattering rate is given by:

$$\Gamma_{\mathbf{k}} = \text{Im}[\Sigma(\mathbf{k}, \epsilon_{\mathbf{k}})], \quad (18)$$

and the quasiparticle spectral weight is given by

$$Z_{\mathbf{k}} = \frac{1}{1 - \text{Re}\left[\frac{\partial \Sigma}{\partial \omega}\right]}. \quad (19)$$

The latter can also be written in terms of the Green's function as,

$$Z_{\mathbf{k}} = -\text{Re}\left[\frac{G(\omega)^2}{\left(\frac{\partial G(\omega)}{\partial \omega}\right)}\right]. \quad (20)$$

Here the derivatives are evaluated at $\omega = \epsilon_{\mathbf{k}}$. For the peak shown in Fig. 2 the fitted peak width led to a value of $Z = 0.490$ while the self-energy derivative led to a value of $Z = 0.477$, showing that the two definitions yield similar, but not identical, values.

IV. FERMI SURFACE LOCATION

In order to discuss how $\Gamma_{\mathbf{k}}$ and $Z_{\mathbf{k}}$ vary on the Fermi surface we need to have a method of precisely determining the position of the Fermi surface. Unfortunately, from the numerical data there are several definitions which are possible, and which produce slightly different shapes.

Figure 3 demonstrates that the maximum in the spectral function, as shown by a minimum in the imaginary part of the Green's function, does not coincide precisely with where the real part of the Green's function is zero. In other words the band energy, $\epsilon_{\mathbf{k}}$, defined by the Lorentzian peak (Eq. 15) differs slightly from the one defined from the self-energy (Eq. 17). There is thus a small ambiguity in the location of the Fermi surface crossing. In order to illustrate this point, Fig. 3 shows the momentum point $(\pi, 3\pi/32)$. Here the spectral function ($A \propto -\text{Im}[G]$) peak is centred at zero, and so by Eq. 15 this momentum is a point in the Fermi surface. On the other hand the real part of the Green's function is not quite zero here, and so this point is not quite at the Fermi surface according to Eq. 17.

A quite different definition of the Fermi surface location can be made in terms of the momentum distribution function $\langle n_{\mathbf{k}} \rangle$. This can be evaluated directly from the Matsubara frequency Green's function

$$\langle n_{\mathbf{k}} \rangle = \frac{1}{2} + \sum_{\omega_n} G(i\omega_n, \mathbf{k}). \quad (21)$$

and so (unlike Eq. 14) can be computed independently of the Padé analytic continuation to real frequencies. In terms of $\langle n_{\mathbf{k}} \rangle$ the Fermi surface corresponds to the discontinuity at zero temperature. However, at finite temperatures $\langle n_{\mathbf{k}} \rangle$ is continuous, and so it is difficult to precisely locate the Fermi surface. A simpler definition, which can be evaluated much more reliably at finite temperatures is the choice $\langle n_{\mathbf{k}} \rangle = 1/2$. In practice we have found that this definition of the Fermi surface is very similar to, but not identical with, the Fermi surfaces defined by $\epsilon_{\mathbf{k}} = 0$. This can be seen in Fig. 4 where the Fermi surfaces arising from the two different definitions, $\epsilon_{\mathbf{k}} = 0$ and $\langle n_{\mathbf{k}} \rangle = 1/2$ are plotted for various densities.

The $\epsilon_{\mathbf{k}} = 0$ Fermi surface is always shifted towards the BZ diagonal $(\pi, 0) - (0, \pi)$ as compared with the $\langle n_{\mathbf{k}} \rangle = 1/2$ Fermi surface, this is due to a flattening of the quasiparticle band around the Fermi surface. This flattening can be easily seen from the band structure as derived from $\epsilon_{\mathbf{k}}$, equation 17. Figure 5 shows the band structure along the BZ path $(0, 0) - (\pi, 0) - (\pi, \pi) - (0, 0)$ for an interacting system, $U = 4t$, and that a non-interacting system with the same density. The interacting band is flatter at the Fermi energy as compared with the non-interacting band. This is especially so around the $(\pi, 0)$ Van Hove saddle point. The $(0, 0) - (\pi, \pi)$ Fermi surface crossing also displays flattening of the band, this makes the Fermi surface crossing a point of inflection in the band structure.

In order to make a definite choice, in the remainder of this paper we define the Fermi surface crossing to be the point where $\epsilon_{\mathbf{k}} = 0$, defining $\epsilon_{\mathbf{k}}$ from the self-energy Eq. 17. We have found that using other definitions leads to essentially the same qualitative behavior. Our conclusions therefore do not depend on the specific definition. In particular all of the results shown in the following section were obtained for both the $\epsilon_{\mathbf{k}} = 0$ and $\langle n_{\mathbf{k}} \rangle = 1/2$ definitions of the Fermi surface and all the qualitative features found were very similar in both cases.

V. TEMPERATURE DEPENDENT QUASIPARTICLE SCATTERING RATE

We have calculated the Hubbard model spectral functions, quasiparticle band parameters and Fermi surface at a wide range of temperatures and band fillings. In this section we present our results for the temperature dependence of the quasiparticle scattering rate $\Gamma_{\mathbf{k}}$. We especially focus on the scattering rate on the Fermi surface, and its dependence on angle around the Fermi surface, θ . For a closed Fermi surface the angle θ was measured from $(0, 0)$, and for an open Fermi surface it was measured from (π, π) .

Below we consider in detail both the nearest neighbor only Hubbard model $t' = 0$, and the next neighbor hopping model with $t' = -0.3t$. As we shall show, the contrast between these two systems helps clarify the different roles played by Fermi surface nesting,

antiferromagnetism and the Van Hove singularity.

A. The $t' = 0$ case

Fig. 6 shows the quasiparticle scattering energy at three different temperatures as a function of angle around the Fermi surface. In this case the chemical potential was set to $\mu = 0$ corresponding to half filling, $\langle n \rangle = 1$. At this filling the Fermi surface is a perfectly nested square. There are two interesting points from Fig. 6. Firstly $\Gamma_{\mathbf{k}}$ has a substantial anisotropy, being about 50% larger at angle $\theta = 0$, the point $(\pi, 0)$, than at $\theta = \pi/2$, the point $(\pi/2, \pi/2)$. This implies that the states near the Van Hove singularity are more heavily scattered than the states near the center of the nested pieces of Fermi surface. The second observation one can make from Fig. 6 is that the scattering rate decreases rather weakly with temperature. On lowering the temperature from $T = 0.25t$ to $T = 0.15t$ $\Gamma_{\mathbf{k}}$ decreases by only about 10 – 20%. This is clearly a non-Fermi liquid temperature dependence. We cannot explore this effect at lower temperatures for this band filling, since the system becomes antiferromagnetic.

In order to go to lower temperatures in the paramagnetic phase it is necessary to go off half filling. Fig. 7 shows the temperature dependent $\Gamma_{\mathbf{k}}$ on the Fermi surface corresponding to $\mu = 0.6t$ ($\langle n \rangle \approx 1.13$). Now both the angular dependence and temperature dependence are quite different. At high temperatures the scattering is maximum around $\theta = 0$, similar to Fig. 6. However at lower temperatures the maximum scattering occurs at $\theta = \pi/2$. In fact at $\theta = 0$ the temperature dependence of $\Gamma_{\mathbf{k}}$ is almost linear. On the other hand, at $\theta = \pi/2$ $\Gamma_{\mathbf{k}}$ is only weakly temperature dependent. In fact $\Gamma_{\mathbf{k}}$ first decreases with decreasing T , but then it has a minimum and starts to increase again. We shall refer to this anomalous behavior as ‘hot spot’ behavior, for reasons which will be clear below. Notice that this behavior allows us to define a temperature scale, T^* , from the position of the minimum in $\Gamma_{\mathbf{k}}$ as a function of T . For example $T^* \approx 0.45t$ in Fig. 7. This T^* may be related to the physical pseudogap behavior seen in ARPES and other experiments in the cuprates.

However we shall always define our T^* from the temperature of the minimum in $\Gamma_{\mathbf{k}}$ rather than from any other specific features in the spectral functions.

Fig. 8 summarizes the temperature dependence of $\Gamma_{\mathbf{k}}$ at the Fermi surface angles $\theta = 0$ and $\theta = \pi/2$ and at different band fillings. One can clearly see that the upturn in $\Gamma_{\mathbf{k}}(T)$ for $\theta = \pi/2$ occurs at a range of band fillings, but that T^* decreases on moving away from half filling. The upturn appears to occur just before entering the antiferromagnetic phase so that $T^* > T_{AF}$. Beyond about $\langle n \rangle > 1.15$ there is no antiferromagnetism and no upturn at all.

Well away from half filling, at $\langle n \rangle = 1.31$, the scattering rate $\Gamma_{\mathbf{k}}$ becomes isotropic. Here the temperature dependence is linear down to a temperature of about $T = 0.06t$. Assuming that $t \approx 0.5\text{eV}$ in the cuprates this would correspond to a temperature of 300K. Below this temperature there is some evidence of a cross over to a T^2 behavior, suggesting that the system is indeed a Fermi liquid. The characteristic temperatures for the observation of Fermi liquid behavior are very much lower than either t , or $J = 4t^2/U$. A linear temperature dependence of $\Gamma_{\mathbf{k}}$ occurs at a wide range of dopings for the Fermi surface angle $\theta = 0$. Since this is the point where the Fermi surface is closest to the Van Hove saddle point, Fig 8 suggests that the linear T dependence of $\Gamma_{\mathbf{k}}$ may be associated with the proximity of the Fermi energy to a Van Hove singularity.

In order to gain further insight into the anisotropy in the scattering rate, Fig. 9 shows a contour plot of $\Gamma_{\mathbf{k}}$, for a quadrant of the BZ at half filling. Here it is seen that the scattering rate actually has a maximum on the FS at the point $(\pi, 0)$. This is definitely unlike a Fermi liquid, for which $\Gamma_{\mathbf{k}}$ goes through a minimum on crossing the Fermi surface. One can see from Fig. 9 that this Fermi liquid minimum of the scattering rate is seen for crossing the FS at the $(\pi/2, \pi/2)$ point.

For a Fermi liquid one also expects the scattering rate to vary as the square of the band energy. Fig. 10 shows the scattering rate as a function of the band energy for densities of $\langle n \rangle = 1$, $\langle n \rangle = 1.19$ and $\langle n \rangle = 1.31$. For each density we have plotted both the maximum and minimum scattering rates $\Gamma_{\mathbf{k}}$ for a given energy $\epsilon_{\mathbf{k}}$. The anisotropy of the scattering

energy is then given by the difference between these two curves. The figure shows that the anisotropy is centered around zero energy for the half-filling case, but moves to lower energy as the density is increased. This indicates that the anisotropy is associated with the Fermi surface proximity to the BZ diagonal or the Van Hove singularity. Once the FS has been moved away from this anisotropic region the energy dependence becomes ω^2 like. From these plots we determine that the system resembles the Fermi liquid model for densities above and including $\langle n \rangle = 1.31$.

B. The $t' = -.3t$ case

We will now compare the results with those from the case when $t' = -.3$. For this case the point where the Fermi surface is at the band saddle point is now at a density of $\langle n \rangle = .75$. Figure 11 shows the scattering rate, $\Gamma_{\mathbf{k}}$, along the Fermi surface for various densities at a temperature of $.06t$. It can be seen that the scattering rate has a maximum between an angle of $\theta = 0$ and $\theta = \pi/2$ unlike the $t' = 0$ case. Figure 12 shows a contour plot of the scattering rate, $\Gamma_{\mathbf{k}}$, for a density of $\langle n \rangle = 1.01$ and a temperature of $T = .03t$. The maximum in the scattering rate is seen to correspond to the point where the FS crosses the BZ diagonal, as previously noted by Altmann Brenig and Kampf [18].

Looking at the temperature dependence of this maximum we can see, Fig. 13, that $\Gamma_{\mathbf{k}}$ increases with decreasing temperature. I.e. it can be described as a ‘hot spot’, and shows a pseudogap T^* behavior. For the lowest temperature, $T = 0.06t$, the maximum in the scattering rate, at angles of about $\theta = \pi/4$ and $\theta = 3\pi/4$, is almost double the value at the minima, at angles of $\theta = 0$ and $\theta = \pi/2$. This enhancement in the scattering rate can also be called a ‘hot spot’ in the sense that it is confined to a small region of the Fermi surface, consistent with the model of Pines and co-workers [17].

Figure 14 shows the temperature dependence of the scattering rate at angles of $\theta = 0$ and $\theta = \pi/2$ and for the maximum value. The scattering rate at $\theta = 0$ and $\theta = \pi/2$ continue to decrease roughly linearly with temperature, and behave quite differently from the T^* upturn

seen at the ‘hot spots’. It also appears that at an angle of $\theta = 0$ and $\theta = \pi/2$ the scattering rate will have a positive intercept at zero temperature, although the zero temperature values cannot be obtained since the system becomes an AFM below $T = .04t$. Plotting the temperature dependence of $\Gamma_{\mathbf{k}}$ at $\theta = 0$ for various densities, see figure 15, it is seen that for densities between $\langle n \rangle = .69$ and $\langle n \rangle = 1.01$ inclusive the temperature dependence is always roughly linear or sublinear with a positive intercept at zero temperature. The positive intercept indicates that the scattering energy is unlikely to cross over to a Fermi liquid T^2 dependence at low temperatures. This might be due to an AFM phase at lower temperatures which we cannot access, or it might indicate a non-Fermi liquid ground state. However for densities outside the region $0.69 < \langle n \rangle < 1.01$ we can say that although the high temperature dependence of the scattering energy is linear, the low temperature dependence could be T^2 . In fact for the densities above $\langle n \rangle = 1.2$ this T^2 behavior can already be seen quite clearly in Fig. 15.

All of the results described so far were obtained using the interaction, $U = 4t$. For this value of U it is difficult to separate the origins of the linear temperature dependence of $\Gamma_{\mathbf{k}}$ near $\theta = 0$ from the effects of the ‘hot spots’ and the proximity to the AFM transition, since they occur at similar doping levels. However, lowering the interaction to $U = 2t$ we are able to separate the various competing physical effects. We can then see that the linear temperature dependence is associated with the Van Hove crossing point and not AFM. Figure 16 shows the temperature dependence of the scattering energy for various densities with $U = 2t$. The density region where there is a linear temperature dependence has now been reduced to a small region around a density of $\langle n \rangle = .76$ which corresponds to the point where the Fermi energy is on the Van Hove singularity in the density of states. For densities above $\langle n \rangle = .91$ and below $\langle n \rangle = .55$ there is a T^2 behavior, or at least a positive curvature at low temperature. For half filling the temperature dependence shows a slight up turn at low temperatures, indicating a ‘hot spot’ with a small T^* , although no AFM phase is observed down to a temperature of $T = .03t$. There are no hot spots at any other filling for $U = 2t$.

As well as the scattering rate displaying linear temperature dependence for densities

around $\langle n \rangle = .76$ the dependence of the scattering rate with band energy, $\epsilon_{\mathbf{k}}$, is also linear. This can be seen in Figure 17 which is for $\langle n \rangle = .76$ and $U = 2t$. For $U = 4t$ the energy dependence of the scattering rate is masked by the increased anisotropy of the system. Despite this the energy dependence of $\Gamma_{\mathbf{k}}$ appears to be linear when the temperature dependence is also linear.

The influence of the Van Hove singularity can be most clearly seen in a plot of the scattering rate as a function of doping, Fig. 18. In this plot the maximum in the scattering energy for $U = 2t$, which occurs at $\langle n \rangle = .76$, is also mirrored by a peak in the scattering energy for $U = 4t$. Although the $U = 4t$ plots are dominated by the enhancements from the Fermi surface ‘hot spots’ occurring near half filling.

VI. CONCLUSIONS

In our calculated quasiparticle scattering rate $\Gamma_{\mathbf{k}}$ we observe two distinct non-Fermi liquid phenomena: regions of linear in temperature dependence of $\Gamma_{\mathbf{k}}$, and ‘hot spots’, a localized increase in the scattering rate with decreasing temperature. Fig. 19 shows the regions of density and temperature at which these two separate phenomena can be observed.

The top panel to Fig. 19 shows relevant regions in the phase diagram of the nearest neighbor Hubbard model with $t' = 0$ and $U = 4t$. The system is symmetrical around half filling and the AFM phase extends to $\langle n \rangle \approx 1 \pm .13$. Near the boundaries of the antiferromagnetic region we observe ‘hot spot’ behavior, and the corresponding pseudogap temperature T^* of the upturn in $\Gamma_{\mathbf{k}}$ is marked on the figure. However one can see from Fig. 19 that Fermi liquid behavior is not recovered outside the region of antiferromagnetism until a density of more than 0.3 away from half filling. For densities between the AFM phase and $\langle n \rangle = 1 \pm 0.3$ $\Gamma_{\mathbf{k}}$ is dominated by a linear temperature dependence.

The second panel in Fig. 19 shows how this behavior is modified by a non-zero t' ($t' = -0.3t$) and the same value of U . In this case the phase diagram is no longer symmetrical. The AFM region is centred just above half-filling, so that the AFM phase is destroyed much

more quickly with p-type as opposed to n-type doping, similar to the experimental behavior in the cuprates. The ‘hot spot’ behavior is now confined to the p-type side of the AFM phase, and Fermi liquid behavior begins immediately after the antiferromagnetism is destroyed for n-type doping. Below half filling there is a wide region of marginal Fermi liquid behavior (MFL on the figure) corresponding to a linear temperature dependence of $\Gamma_{\mathbf{k}}$. This MFL region is centered around the Van Hove singularity and extends down as far as $\langle n \rangle \sim 0.5$.

Finally, the bottom panel in Fig. 19 shows the behavior at the smaller value of $U = 2t$ and the same value of $t' = -0.3t$. Here the antiferromagnetism has essentially disappeared, as has the ‘hot spot’ behavior. On the other hand there is still a MFL region, which is very clearly centered on the van Hove singularity at $\langle n \rangle = 0.75$.

Our calculations have ramifications for a number of the current theories of high temperature superconductivity. Firstly the observations of ‘hot spots’, with a corresponding pseudogap temperature scale, T^* , supports the concepts of *hot-* and *cold-quasiparticles* as advocated by Pines and others [17]. We find that this behavior is a consequence of the proximity to the AFM phase, and would be especially pronounced in the underdoped p-type cuprates (assuming that the physical parameters are roughly similar to those of the central panel in Fig. 19), as is indeed the case experimentally. From the calculations described in this paper we indeed see that the ‘hot spots’ are associated with quasiparticles with increased scattering located near the singular points on the Fermi surface connected by the AFM wave vector Q_{AF} , as also noted previously by Altmann, Brenig and Kampf [18].

On the other hand, the ‘hot spot’ behavior appears to be unrelated to the MFL behavior ($\Gamma_{\mathbf{k}} \sim T, \epsilon_{\mathbf{k}}$) which we also observe. The parameter region where these *hot-quasiparticles* occur is confined to a small region near to the AFM transition, and the temperature dependence of the scattering rate of the ‘hot spot’ quasiparticles is not linear in temperature. We observe MFL behavior over a much wider region of parameter space than the ‘hot spots’. For $U = 4t$ the MFL and hot spot behavior may occur at the same band fillings, but on different pieces of Fermi surface. However for band fillings further away from the AFM phase only MFL is observed. For $U = 2t$ both the AFM and the ‘hot spot’ behavior are

suppressed, showing clearly that the MFL behavior originates in the proximity to the Van Hove singularity not the AFM. This observation is in agreement with the scattering rate predictions of the 'Van Hove scenario' theories of the cuprates [27].

Note that we have only performed normal-state calculations, and so have not included any possible d-wave superconducting phases in Fig. 19. We cannot therefore comment on the existence of superconductivity induced by spin fluctuations near to the AFM phase boundary [17] or whether the Van Hove singularity also plays a role in enhancing the superconductivity [27].

In summary we find that the Van Hove singularity produces marginal Fermi liquid behavior, scattering rates linearly dependent on temperature, while the AFM phase is associated with *hot-quasiparticles*. These *hot-quasiparticles* are characterised by increasing scattering rates with decreasing temperature, have a characteristic pseudogap temperature scale T^* , and are localized to a small region of the BZ near the points where the Fermi surface crosses the diagonal and are connected by the antiferromagnetic wave vector Q_{AF} .

ACKNOWLEDGMENTS

We would like to thank B.L. Györfly for stimulating discussions. This work has been supported by the Office of Naval Research Grant No. N00014-95-1-0398.

REFERENCES

- [1] J. Hubbard, Proc. Roy. Soc. (London) **A276**, 238 (1963).
- [2] W.F. Brinkman and T.M. Rice, Phys. Rev. B **2**, 4302 (1970).
- [3] J.E. Hirsch, Phys. Rev. B **31**, 4403 (1985).
- [4] C. Gross, R. Joynt and T.M. Rice, Z. Phys. B **68**, 425 (1987).
- [5] G. Baskaran, Z. Zou and P.W. Anderson, Solid State Commun. **63**, 973 (1987).
- [6] P.W. Anderson, Phys. Rev. Lett. **64**, 1839 (1990).
- [7] I. Affleck and B. Marston, Phys. Rev. B **37**, 3774 (1988).
- [8] C.M. Varma *et al.*, Phys. Rev. Lett. **63**, 1996 (1989).
- [9] J.F. Annett, N. Goldenfeld and A.J. Leggett, in “Physical Properties of High Temperature Superconductors V”, D.M. Ginsberg (ed.) (World Scientific, Singapore 1996).
- [10] S.B. Bacci, E.R. Gagliano, R.M. Martin and J.F. Annett, Phys. Rev. B **44**, 7504 (1991).
- [11] N.E Bickers and D.J. Scalapino, Ann. of Phys. **193**, 206-251 (1989).
- [12] N.E.Bickers, D.J.Scalapino and S.R.White, Phys. Rev. Lett. **62**,961 (1989).
- [13] J.J.Deisz, D.W.Hess and J.W.Serene, Phys.Rev.Lett. **76**,1313 (1996).
- [14] N.E.Bickers and S.R.White, Phys.Rev.B **43**, 8044 (1991).
- [15] Kenji Yonemitsu, J. Phys.Soc.Jpn. **58** 4576 (1989).
- [16] Gordon Baym, Phys.Rev. **127**, 1391 (1962).
- [17] A. Sokol and D. Pines, Phys. Rev. Lett. **71**, 2813, (1993); P. Monthoux and D. Pines, Phys. Rev. B **50**, 16015 (1994); D. Pines, Z. Phys. B to be published; D.Pines, cond-mat/9707267.
- [18] J. Altmann,W. Brening and A.P. Kampf,cond-mat/9707267.

- [19] C.C. Holmes *et al.* Phys. Rev. Lett. **71**, 1645 (1993); A.V. Puchkov, D.N. Basov, and T. Timusk, J. Phys.: Condens. Matter **8**, 10049 (1996).
- [20] T.E. Mason *et al.* Phys. Rev. Lett. **77**, 1604 (1996).
- [21] H. Ding *et al.*, Science **382**, 51 (1996).
- [22] O.K. Andersen, O. Jepsen, A.I. Liechtenstein and I.I. Mazin, Phys. Rev. B **49**, 4145 (1994).
- [23] D.M. Newns, C.C. Tsuei and P.C. Pattanik, Phys. Rev. B **52**, 13611 (1995).
- [24] B.L. Györffy, Z. Szotek, W.M. Temmerman, O.K. Andersen and O. Jepsen, unpublished.
- [25] H.J. Vidberg and J.W. Serene, J. Low Temp. Phys. **29**, 179 (1977).
- [26] Z.-X. Shen and J.R. Schrieffer, Phys. Rev. Lett. **78** 1771 (1997).
- [27] D.M. Newns, P.C. Pattnaik, and C.C. Tsuei, **43**, 3075 (1991).

FIGURES

FIG. 1. Spectral functions for momentum points along the lines $(0,0) - (\pi,0)$ (a) , $(\pi,0) - (\pi,\pi)$ (b) , and $(0,0) - (\pi,\pi)$ (c). The calculations were for $t' = 0$, $U = 4t$, $T = .1t$ and $\langle n \rangle = 1.08$.

FIG. 2. Spectral function $A(\mathbf{k},\omega)$ for momentum point $(\pi, 5\pi/32)$ from FLEX calculations compared with that derived from the approximate form of Eq. 15, where $\Gamma = .36737t$, $Z = .490$ and $\epsilon_{\mathbf{k}} = .074t$. These values were taken from the height and the half width, using the derivative of the Green's function, as in equation 20, $Z = .477$.

FIG. 3. Plot of the real and imaginary components of the self-energy and the Green's function for a momentum point of $(\pi, 3\pi/32)$. This is the nearest momentum point to the Fermi surface crossing. The other parameters of the plot are $t' = 0$, $U = 4t$, $T = .1t$ and $\langle n \rangle = 1.08$. For this plot the real part of the Green's function is zero at a frequency of $-.013t$, the minimum in the imaginary part of the Green's function is at $.006t$ and the maximum in the imaginary part of the self-energy is at $.106t$.

FIG. 4. Fermi surfaces defined as $\langle n_{\mathbf{k}} \rangle = .5$, solid lines, and $\epsilon_{\mathbf{k}} = 0$, dashed lines for densities of $\langle n \rangle = .54, .61, .81, 1.01, 1.2, 1.3$.

FIG. 5. Band structure from $\epsilon_{\mathbf{k}}$, equation 17 for $t' = -.3t$, $T = .03t$, $\langle n \rangle = .81$ and $U = 4t$ and $U = 0$.

FIG. 6. Scattering rate, $\Gamma_{\mathbf{k}}$, as a function of the angle along the Fermi surface, θ , for temperatures of $T = .15t$, $T = .2t$ and $T = .25t$. Other parameters being $t' = 0$, $U = 4t$ and $\langle n \rangle = 1$.

FIG. 7. Scattering rate, $\Gamma_{\mathbf{k}}$, as a function of the angle along the Fermi surface, θ , for temperatures of $T = .03t$ to $T = .06t$. Other parameters being $t' = 0$, $U = 4t$ and $\mu = .6t$ ($\langle n \rangle \approx 1.13$) . In this plot the scattering energy for $T = 0.3t$ is higher around the $\pi/2$ angle that that for higher temperatures, this is typical 'hot spot' behavior.

FIG. 8. Temperature dependence of the scattering rate, $\Gamma_{\mathbf{k}}$, for $t' = 0$, $U = 4t$, and an angle along the Fermi surface of $\theta = 0$ and $\theta = \pi/2$. The plots for various densities show that the temperature dependence is nearly linear for a wide range of densities with a positive intercept at zero temperature for densities below $\langle n \rangle = 1.19$.

FIG. 9. Contour plot of the scattering energy, $\Gamma_{\mathbf{k}}$, as a function of Brillouin zone position, for $t' = 0$, $U = 4t$, $T = .25t$ and $\langle n \rangle = 1$. The saddle points at $(\pi, 0)$ and $(0, \pi)$ are not at a minimum of the scattering energy and show enhanced scattering there. In this plot the contours are only shown in the region close to the Fermi surface, which in this case is the diagonal from $(\pi, 0)$ to $(0, \pi)$.

FIG. 10. Plot of the scattering rate, $\Gamma_{\mathbf{k}}$, versus the band energy, $\epsilon_{\mathbf{k}}$, for momentum points along the path $(0, 0) - (\pi, 0) - (\pi, \pi) - (0, 0)$ and with $t' = 0$, $U = 4t$, $T = .1t$ and densities of $\langle n \rangle = 1, 1.19, 1.31$. The two lines for each plot roughly correspond to the maximum and minimum values of the scattering rate for a particular energy. These plots show clear deviation from Fermi liquid behavior since the scattering rate is not proportional to the square of the band energy. The separation of the lines gives an indication of the anisotropy of the scattering rate. For the $\langle n \rangle = 1.31$ plot the scattering rate no longer has a large anisotropic region and although the energy dependence is steeper on the negative energy side the behavior is more Fermi liquid like.

FIG. 11. Scattering rate, $\Gamma_{\mathbf{k}}$, as a function of the angle along the Fermi surface, θ , for densities from $\langle n \rangle = .54$ to $\langle n \rangle = 1.3$, other parameters being $t' = -.3t$, $U = 4t$, and $T = .06t$. The scattering rate is maximum for $\langle n \rangle = 1.05$ while the antiferromagnetic ordering region occurs between $\langle n \rangle = 1.1$ and $\langle n \rangle = 1.2$.

FIG. 12. Contour plot of the scattering rate, $\Gamma_{\mathbf{k}}$, as a function of Brillouin zone position, for $t' = -.3t$, $U = 4t$, $T = .1t$ and $\langle n \rangle = 1$. The ‘hot spots’ can be clearly seen on the diagonal of the BZ. The solid crossing line is the Fermi surface.

FIG. 13. Scattering rate, $\Gamma_{\mathbf{k}}$, as a function of the angle along the Fermi surface, θ , for temperatures from $T = .06t$ to $T = .14t$, other parameters being $t' = -.3t$, $U = 4t$, $\mu = -.4$ ($\langle n \rangle \approx 1.01$). The 'hot spots' can clearly be seen at angles of $\pi/4$ and $3\pi/4$, where the scattering rate increases with lowering temperature.

FIG. 14. Temperature dependence of the scattering rate, $\Gamma_{\mathbf{k}}$, for $t' = -.3t$, $U = 4t$, $\langle n \rangle = 1.01$. The plots drawn show the scattering rate at angles along the Fermi surface of $\theta = 0$ and of $\theta = \pi/2$ and also shown is the maximum scattering rate, which for this case occurs at an angle of about $\theta = \pi/4$. At this angle the scattering rate increases with decreasing temperature, evidence for a 'hot spot' on the Fermi surface.

FIG. 15. Temperature dependence of the scattering rate, $\Gamma_{\mathbf{k}}$, for $t' = -.3t$, $U = 4t$, and an angle along the Fermi surface of $\theta = 0$. The plots for various densities show that the temperature dependence is nearly linear for a wide range of densities with a positive intercept at zero temperature for all densities between $\langle n \rangle = .54$ and $\langle n \rangle = 1.2$.

FIG. 16. Temperature dependence of the scattering rate, $\Gamma_{\mathbf{k}}$, for $t' = -.3t$, $U = 2t$, and an angle along the Fermi surface of $\theta = 0$. The plots for various densities show that the temperature dependence is nearly linear only for a few values of the density with the maximum scattering occurring at $\langle n \rangle = .76$. At this density the Fermi energy is at the Van Hove singularity in the density of states.

FIG. 17. Plot of the scattering rate, $\Gamma_{\mathbf{k}}$, as a function of band energy, $\epsilon_{\mathbf{k}}$, for all momentum points (dots) for $t' = -.3$, $U = 2t$, $\langle n \rangle = .76$ and $T = .03t$. The line connects the points on the path $(0, 0) - (\pi, 0) - (\pi, \pi) - (0, 0)$ in the BZ.

FIG. 18. Scattering rate, $\Gamma_{\mathbf{k}}$, as a function of density for an interaction strength of $U = 4t$ at an angle along the Fermi surface of $\theta = 0$ and $\theta = \pi/2$ and for an interaction strength of $U = 2t$ at an angle along the Fermi surface of $\theta = 0$. Other parameters being $t' = -.3t$ and $T = 0.6t$.

FIG. 19. Rough sketch of the phase diagram, showing the regions of temperature and density at which we see Fermi liquid behaviour (FL), marginal Fermi liquid behavior (MFL), AFM ordering and T^* the characteristic temperature at which ‘hot spots’ occur. The top graph is for $t' = 0$ and $U = 4t$, the middle graph is for $t' = -.3t$ and $U = 4t$ and the bottom graph is for $t' = -.3t$ and $U = 2t$.

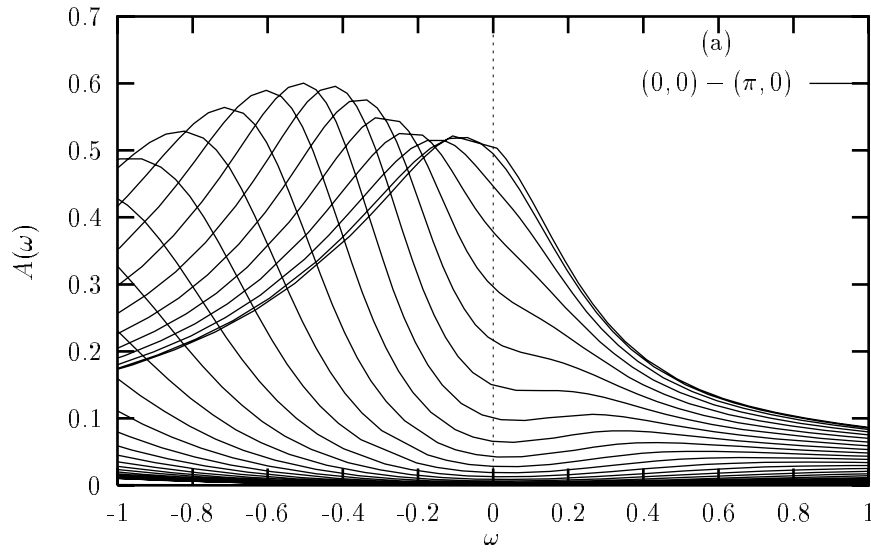


Figure 1: (a) W.H.Beere & J.F.Annett

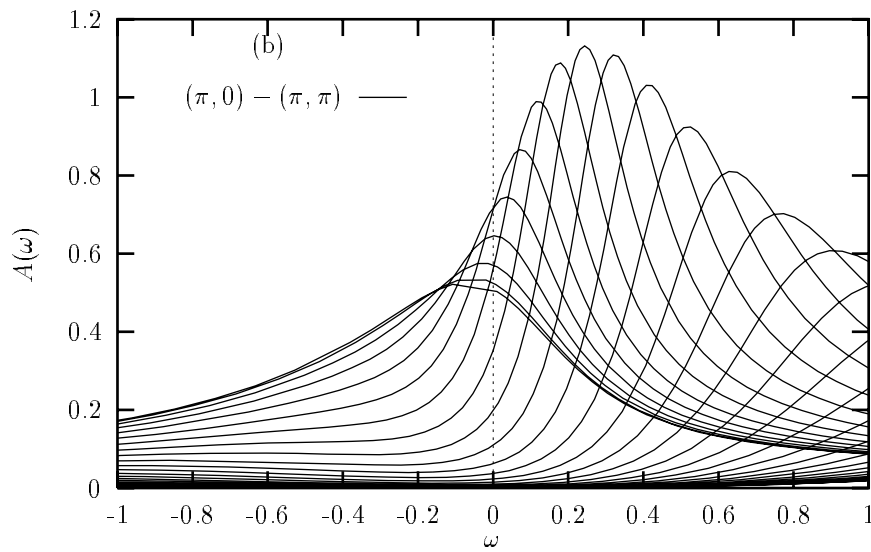


Figure 1: (b) W.H.Beere & J.F.Annett

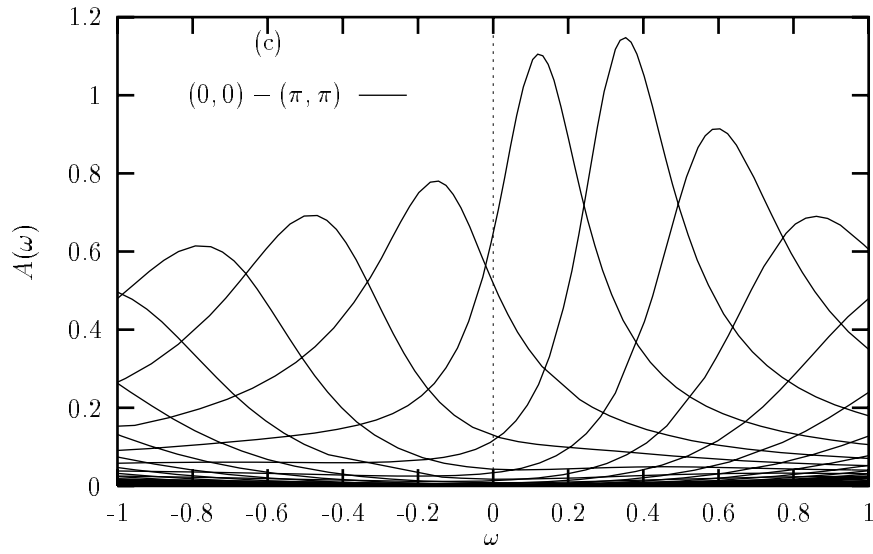


Figure 1: (c) W.H.Beere & J.F.Annett

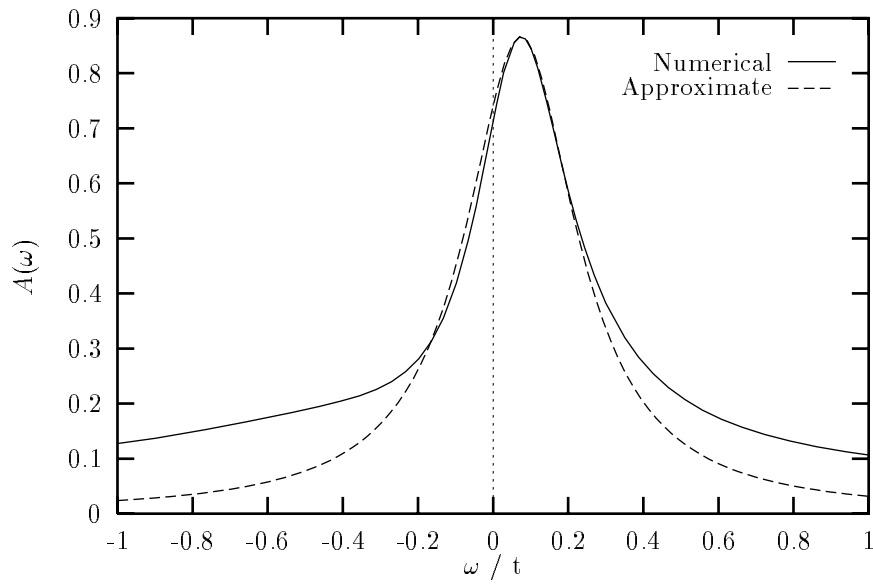


Figure 2: W.H.Beere & J.F.Annett

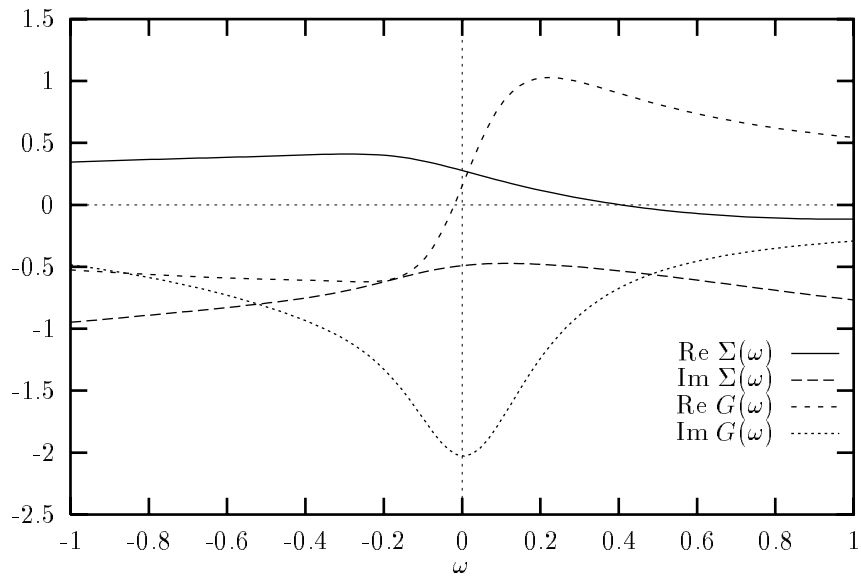


Figure 3: W.H.Beere & J.F.Annett

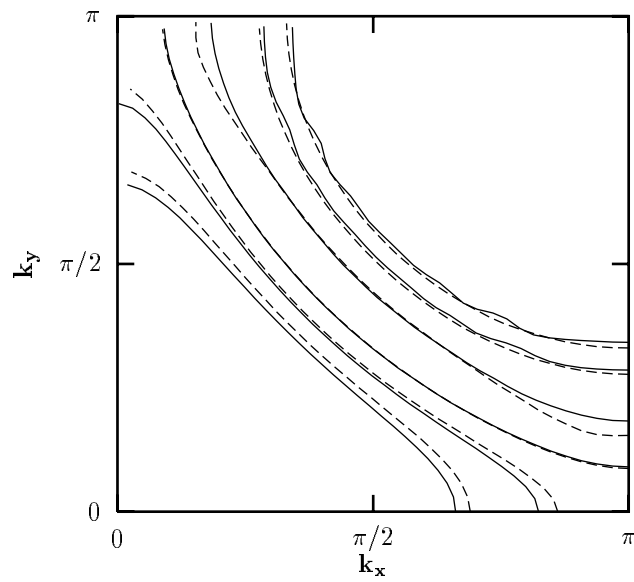


Figure 4: W.H.Beere & J.F.Annett

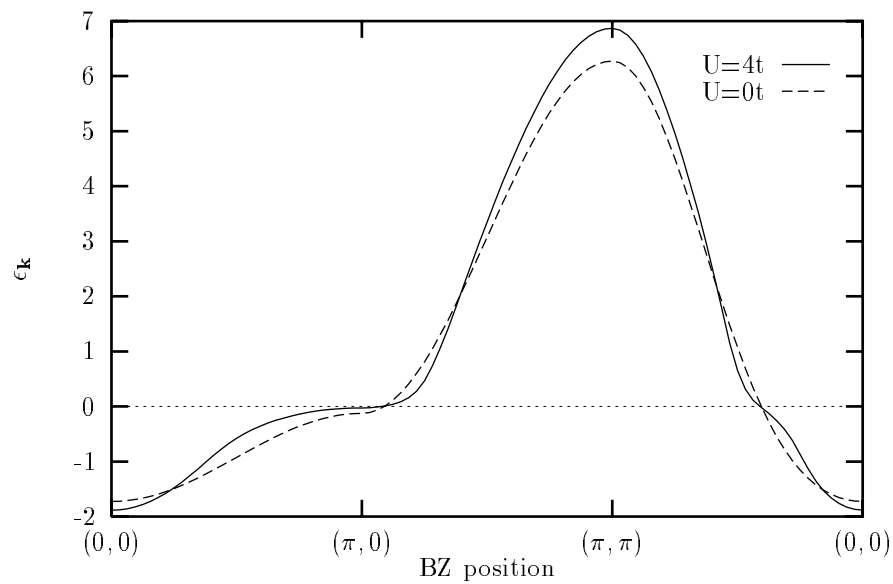


Figure 5: W.H.Beere & J.F.Annett

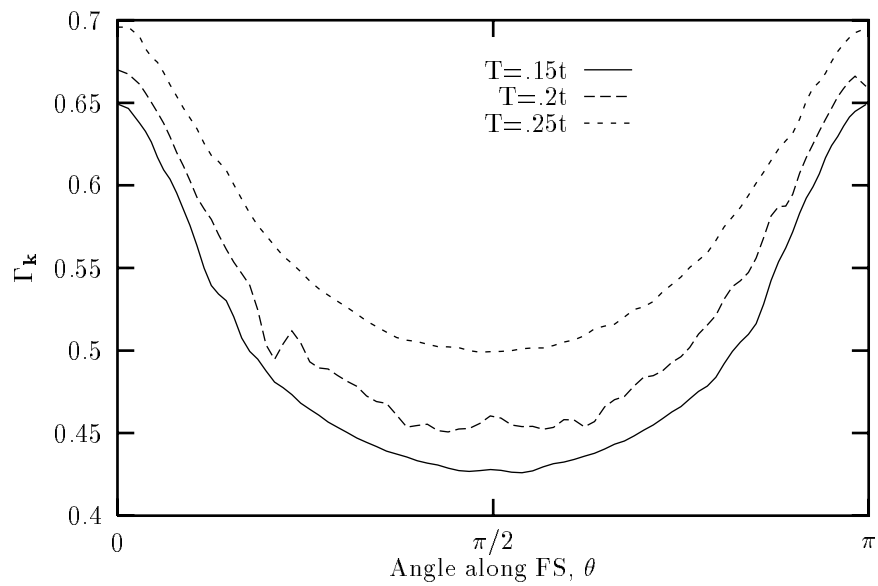


Figure 6: W.H.Beere & J.F.Annett

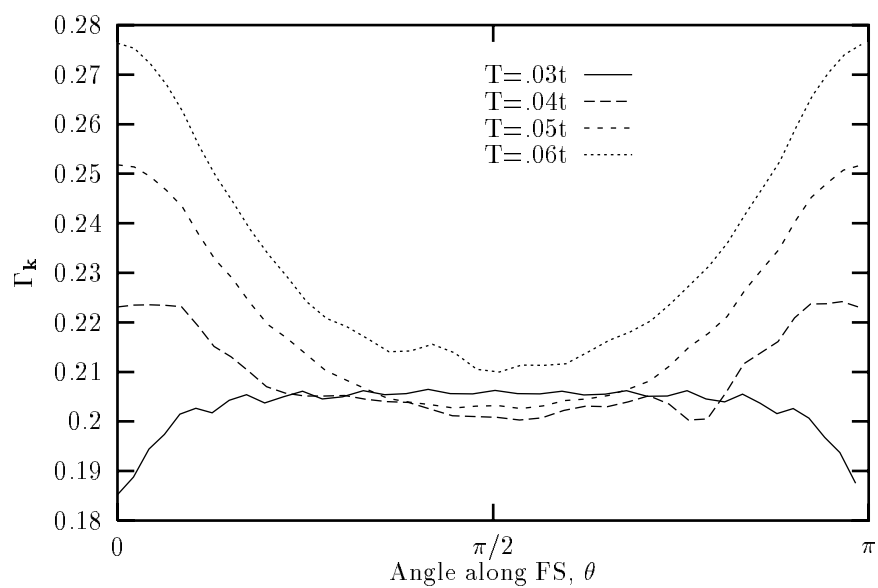


Figure 7: W.H.Beere & J.F.Annett

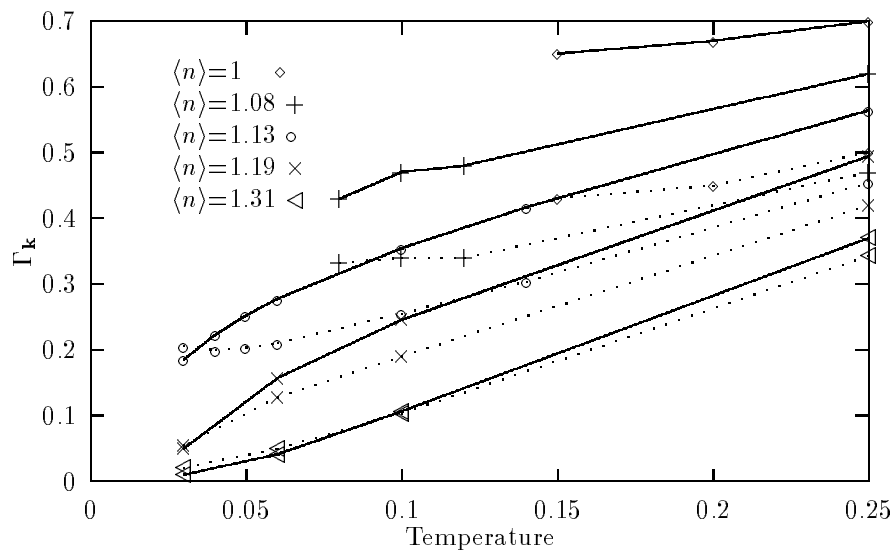


Figure 8: W.H.Beere & J.F.Annett

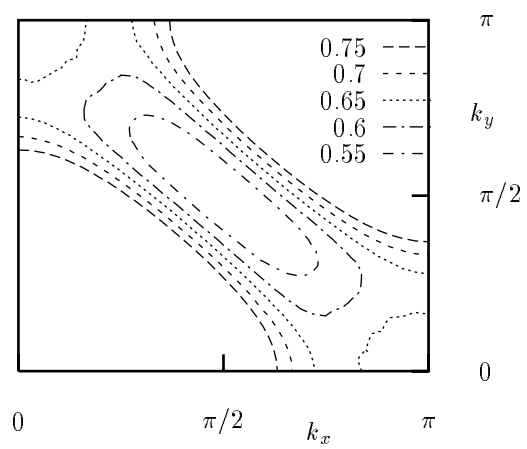


Figure 9: W.H.Beere & J.F.Annett

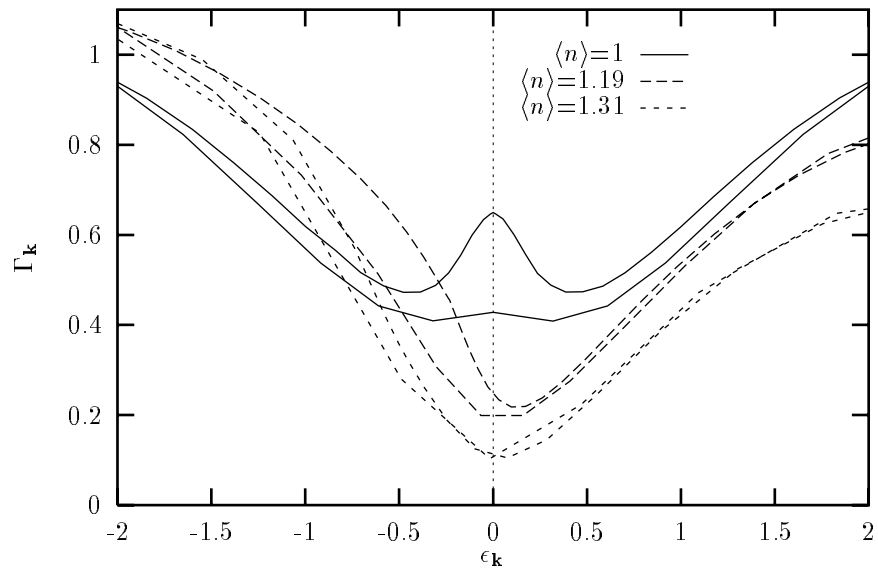


Figure 10: W.H.Beere & J.F.Annett

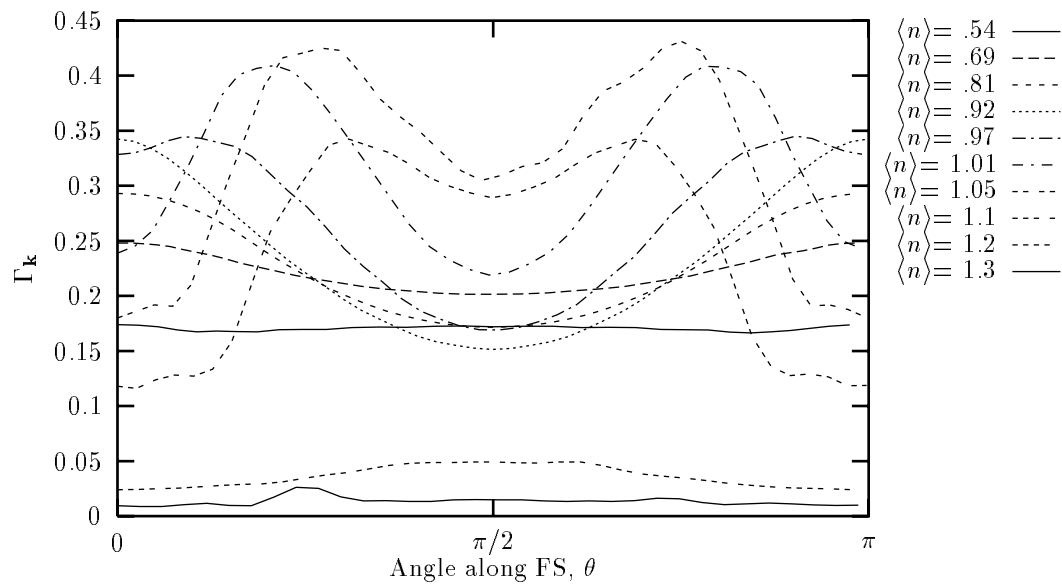


Figure 11: W.H.Beere & J.F.Annett

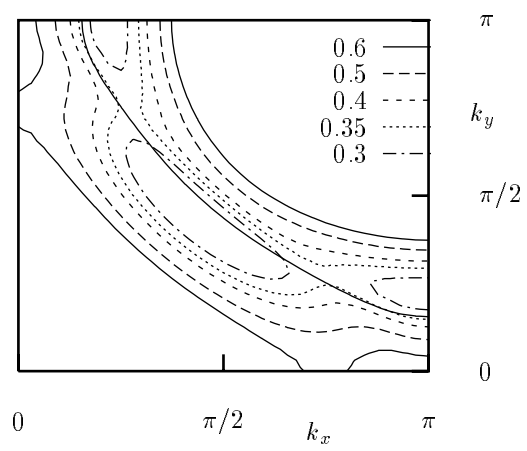


Figure 12: W.H.Beere & J.F.Annett

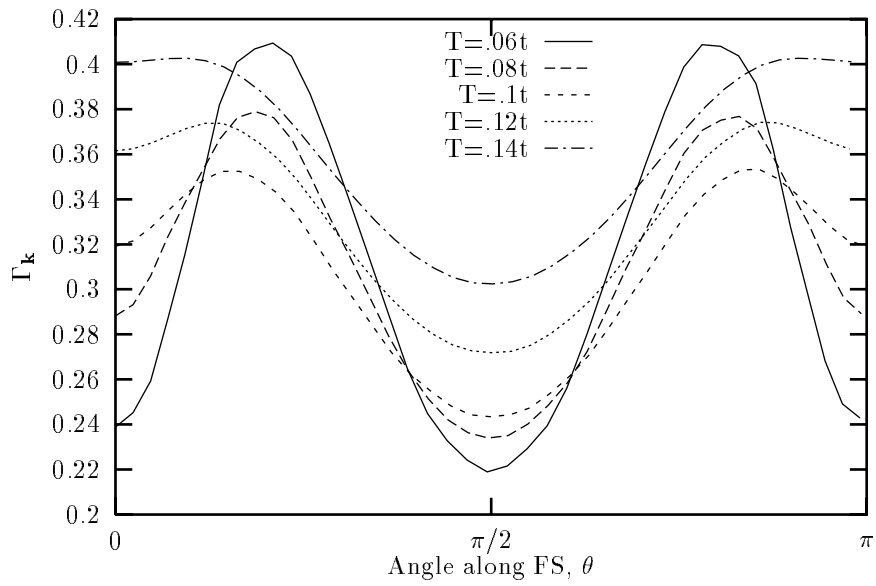


Figure 13: W.H.Beere & J.F.Annett

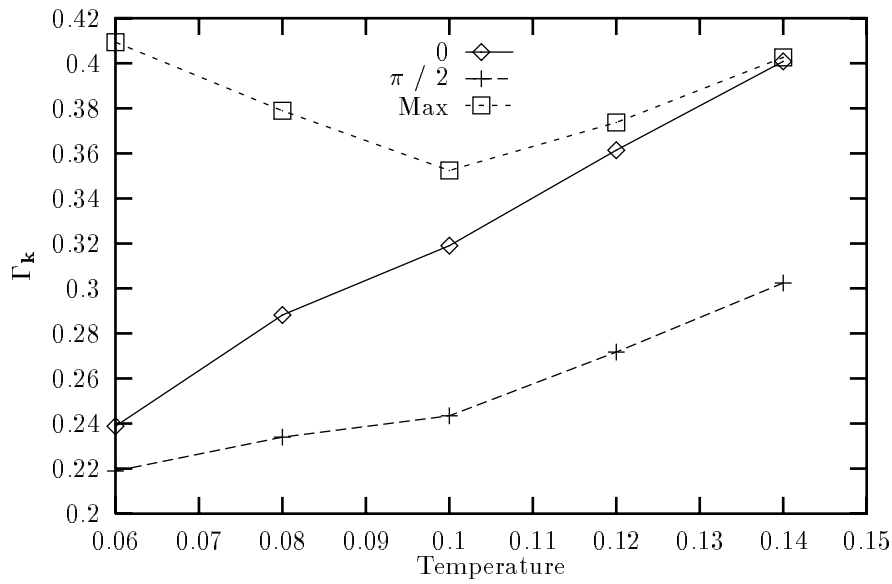


Figure 14: W.H.Beere & J.F.Annett

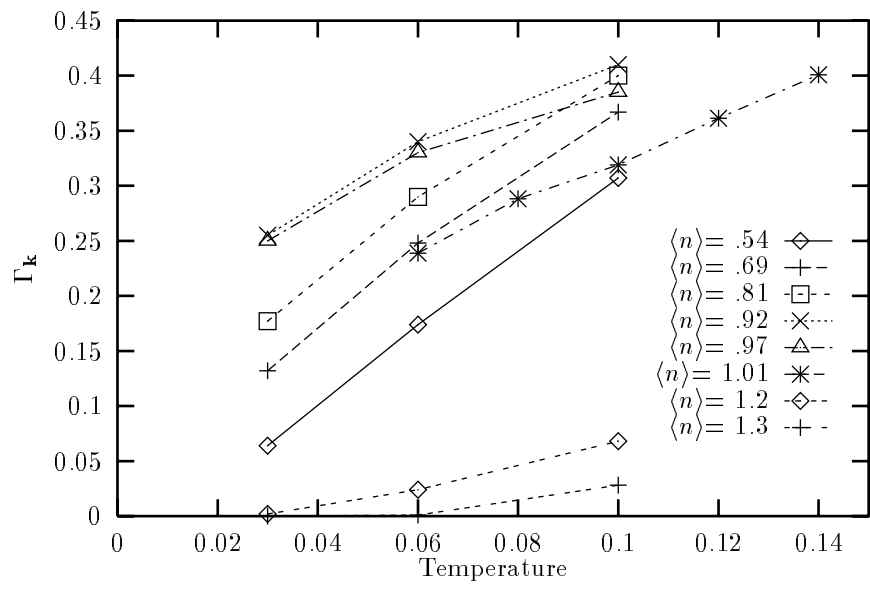


Figure 15: W.H.Beere & J.F.Annett

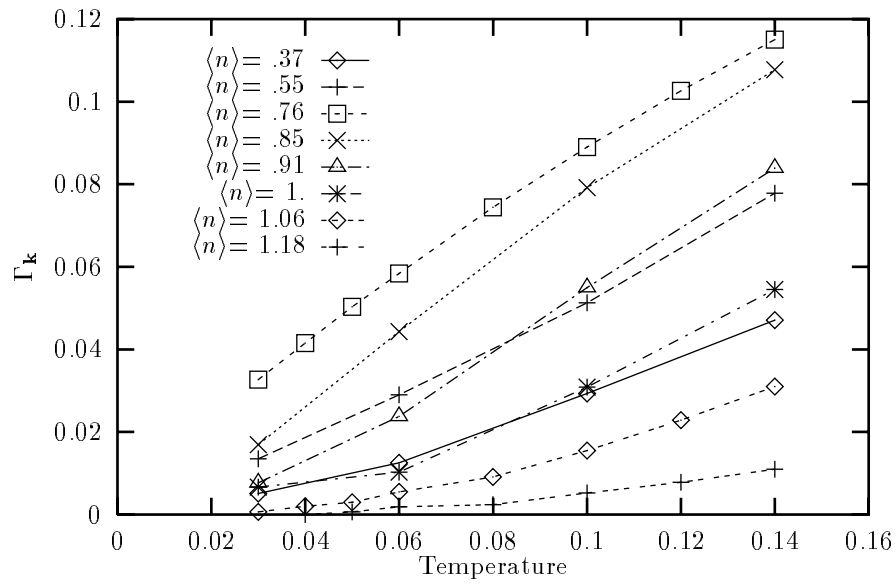


Figure 16: W.H.Beere & J.F.Annett

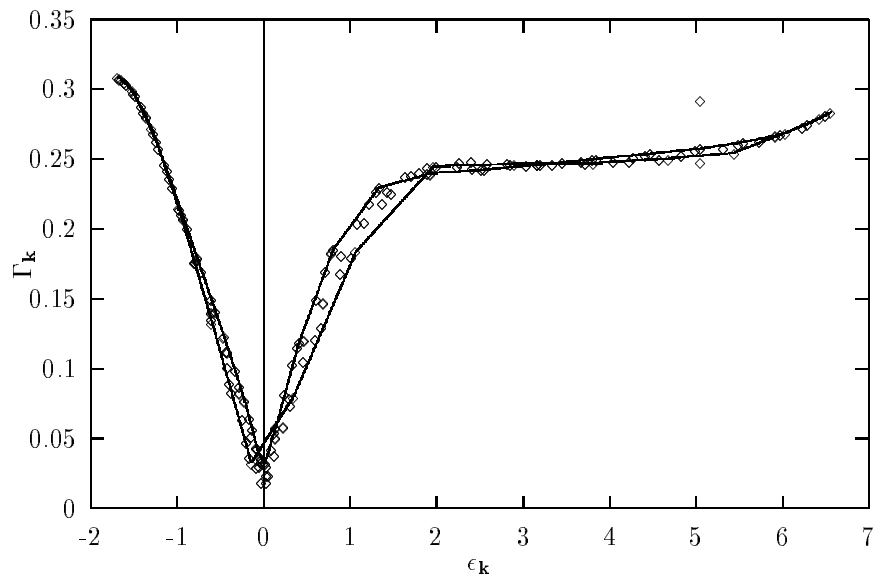


Figure 17: W.H.Beere & J.F.Annett

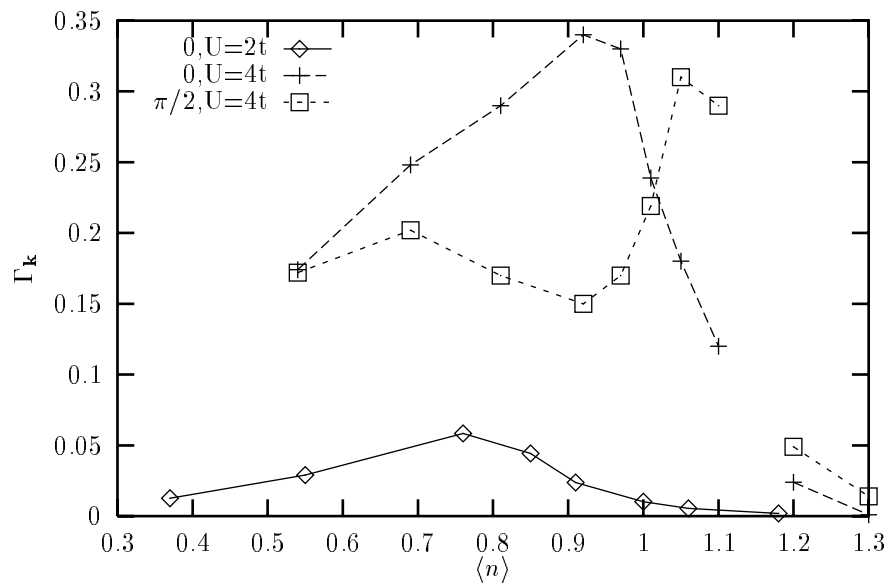


Figure 18: W.H.Beere & J.F.Annett

